JOINT INVERSION OF SEISMIC TRAVELTIMES AND GRAVITY DATA ON THE MICANG FORELAND FOLD BELT AND ITS HYDROCARBON POTENTIAL

YUSHAN YANG and YUANYUAN LI

Institute of Geophysics and Geomatics, China University of Geosciences (Wuhan), Wuhan 430074, Hubei, P.R. China. samyys@126.com

(Received September 9, 2013; revised version accepted December 18, 2013)

ABSTRACT

Yang, Y. and Li, Y., 2014. Joint inversion of seismic traveltimes and gravity data on the Micang foreland fold belt and its hydrocarbon potential. *Journal of Seismic Exploration*, 23: 41-63.

The Micang foreland fold belt is a transitional zone between the Qinling orogen and Sichuan Basin. Affected by multi-stage tectonic processes and complicated driving forces, the Micang foreland fold belt can not be successfully traced in the seismic sections, due to its complex geological structures. We present a detailed 2D density and velocity transects for the upper crust across the Micang foreland belt using a joint seismic reflection and gravity inversion technique. We use a weighted least square scheme to simultaneously invert the density and velocity. This technique parameterizes the crust as a set of layers that are based on published geologic and seismic models. Each layer has a uniform density and velocity that are constrained where possible by borehole measurements, seismic velocities, and petrologic data. Then the joint inversion of travel time and gravity data is performed to find out a common model having an optimum fit of both travel time and gravity data. Since the global misfit is the addition of the contribution of the two methods, we add a weighting factor in the objective function to better coordinate these two different kinds of data. After being tested with a multi-layered model, the joint inversion scheme is adopted for the Micang foreland belt to construct a more complete upper crustal image. We finally discuss the presence of the overthrusted structure in terms of interaction between the Qinling orogen and Sichuan Basin.

KEY WORDS: joint inversion, gravity, seismic data, Micang foreland fold belt.

INTRODUCTION

Located at a transitional position between the Qinling orogen and Sichuan Basin, the Micang anticlinorum and its foreland fold belt is of great significance

0963-0651/14/$5.00

for revealing the coupling process of these two distinct different structures (Dong et al., 2011). Moreover, the foreland fold and thrust belt is always *reported to have great potential* in hydrocarbon resources. For instance, the oil fields are discovered to be distributed along the east-thrusting folded belts in the foreland belt of the Rocky Mountains. Similar exploration experiences can also be observed in Venezuela, Colombia and many other South American countries (Platt et al., 1984; McClay, 1992). China has also witnessed great achievements in the foreland belt reservoir exploration in the Junggar and Qaidam (Liu et al., 2007). However, although widely distributed, the foreland fold belt are generally in complex tectonic conditions, which is a major hurdle for the successful imaging in the seismic sections.

The subsurface structures typically have different physical properties, and in case these properties are correlated, a joint inversion scheme can be adopted to mitigate the restrictions inherent to the single data sets. Moreover, the number of independent observations is increased. After the inversion the resulting model should be able to explain both data sets leading to a reduced space of possible solutions and a *less ambiguous* and stable model. Here, seismic reflection traveltime and gravity data are used to obtain models of velocity and density with respect to the respective background model. This combination is advantageous especially for the study area without reliable seismic data, since the data complement each other.

Cooperative inversions of geophysical data have been introduced by Lines et al. (1988). The aim of this concept is to obtain a geophysical model consistent with multiple datasets. Two different philosophies have been defined depending on the inversion procedure: sequential or joint inversion. In the sequential approach, the inversion for a particular data set provides the input or initial model estimate for the inversion of a second data set; joint inversion treats all the datasets simultaneously. However, in this second process, *the misfit errors for each data set must be given a weighting*.

Whichever approach is used, the user faces the difficulty of solving the inverse problem and thus the choice of an adapted algorithm. Classically, during the past decades, most geophysical inverse problems were solved by inverting matrices using methods such as weighted least-squares analysis (e.g., Menke, 1984; Aki et al., 1977). Joint inversions of geophysical data in general were developed following this procedure (e.g., Julia et al., 2000; Parsons et al., 2001; Tikhotsky and Achauer, 2008; Maceira and Ammon, 2009).

We have combined the seismic reflection traveltime data with existing gravity data in a joint inversion scheme to estimate both P-wave velocity and density structure beneath the Micang foreland belt. The new picture of the margin's structure provides news highlights on the interaction between the Qinling orogen and Sichuan Basin and related margin's formation.

TECTONIC AND GEOLOGICAL SETTINGS

The Micang anticlinorum and its foreland belt is a nearly E-W striking nappe structure, surrounded by the Qinling orogen in the north, Sichuan Basin in the south, Daba faulted fold belt in the east and Longmenshan structural belt in the west (Fig. 1). The Micang anticlinorum and its foreland are located at the boundary zone between the NCC and the Yangtze craton, therefore the Paleo-Tethys Ocean, the evolution of Qinling orogen, as well as the interaction between the Yangtze craton and North China craton have significant imprints on its geological history.

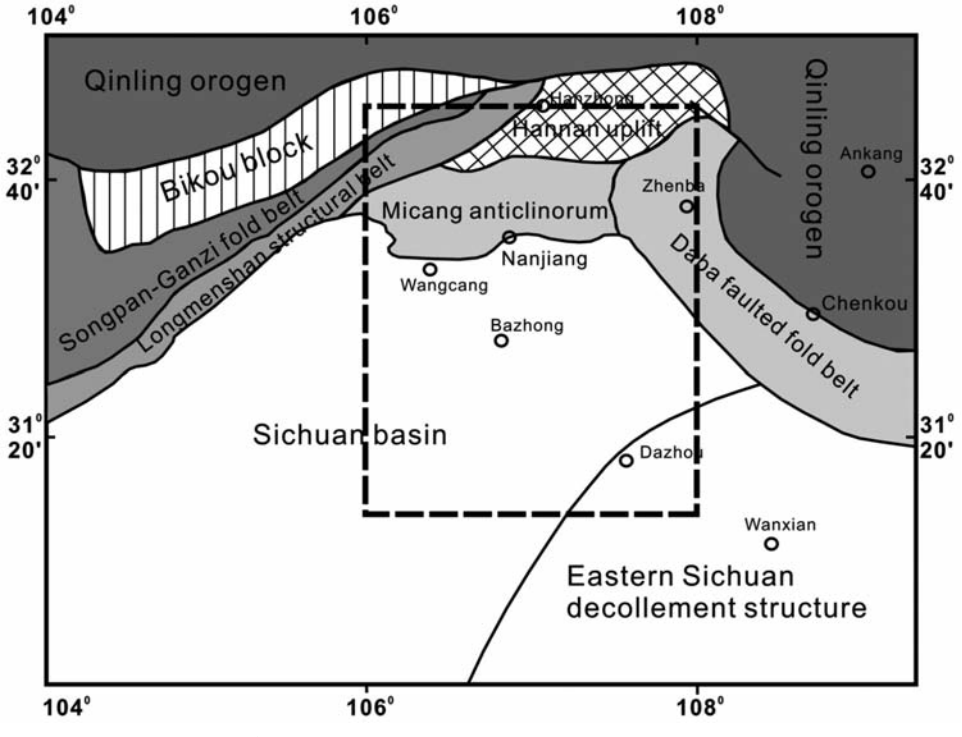

Fig. 1. Simplified geological map (modified from Sun, 2011) for the main structural units in our study area (indicated in dashed rectangle). The Micang anticlinorum and Micang foreland basin are in the north-central of our map.

The Chinese continent experienced intracontinental rifting in the early and middle Proterozoic, and a later convergence process in the new Proterozoic (Gao, et al., 1996). In the early Sinian, the Paleo-Tethys Ocean formed along the Shangdan suture to separate the North China craton and Southern Qinling block (Meng and Zhang, 1999, 2000). Since the Ordovician, the outstretched

Qinling Ocean subducted to the north, generating the active continent margin, together with the fore-arc and back-arc basins in the southern edge of North China craton (Sun et al., 1996). From the middle Silurian to Devonian, the North China craton collided with the southern Qinling block, developing relic basins and collision -type granites (Zhang et al., 1997). Then in the D_{2-3}-C_1, the Paleo-Tethys Qinling Ocean closed, and the Mianlue Ocean began to open. From P_3-T_2, the ocean crust subducted and diminished. Finally in the T_{2-3}, the orogen formed from continent-continent collision (Meng and Zhang, 2000; Liu et al., 2001; Zhang et al., 2004).

In the late Triassic, intracontinental deformation occurred in the northern margin of Yangtze block. The Yangtze block rotated clockwise (Lin et al., 1985; Zhao and Coe, 1987), and in the Longmenshan area, the inland subduction westward and sinistral strike-slip of the Yangtze block was observed (Liu et al., 2009). Due to the collisional orogenesis of the Qinling Mountains, the folded thrust structures and foreland basins were formed from north to the south in the Micang mountains (Liu, 1993; Li, 2006; Liu et al., 2006). Since the Mesozoic, the lower crust flow beneath the Tibet Plateau has been hypothesized, which is suggested to be related with the collision between the India and Euroasia plate (Clark and Royden, 2000; Enkelmann et al., 2006; Harris, 2007; Lee and Whitehouse, 2007; Jess King et al., 2007). One of the consequences of the flow is the progressive uplift of the Longmenshan area from the southwest to the northeast (Liu et al., 2009), which also lead to the uplift of the Sichuan Basin and its surrounding orogens, such as the Michang mountains (Deng et al., 2008).

The main geological units can be roughly identified in the Bouguer gravity map (Fig. 2b). Located in the northwest corner of our study area, the Ningqiang foreland thrust fold belt is composed of a series of NEE folds and thrust faulted structures. In the Bouguer gravity map, it has alternative gravity highs and lows. *Moving to the east*, there is a prominent gravity low in the Hannan uplift. According to the surface geology, it may be associated with the low-density granites exposed on the surface. Located at the south of the Hannan uplift, the Micang anticlinorum corresponds to an obvious gravity high in the Bouguer gravity map. In this region, the crystalline and metamorphic basements in the late Archean and Proterozoic period have been observed in the earth surface, which are assumed to the sources of gravity high. In the southwest of our study area, the wide Sichuan Basin has gravity high in the middle, which is probably the reflection of its dome-like structure.

Besides the ground measurements, seismic reflection surveys have also been conducted in our study area since 2004 (profiles can be seen in Fig. 2). However, the high topography (about 1000～2000 m, Fig. 2a) and complex geological structures in the Micang foreland belt, always make the seismic observations complicated, not even to mention the following-up geological

interpretations. We address these issues by performing a joint inversion of gravity and seismic data to quantitatively and efficiently take advantage of both data sets and locate the common sources within the crust.

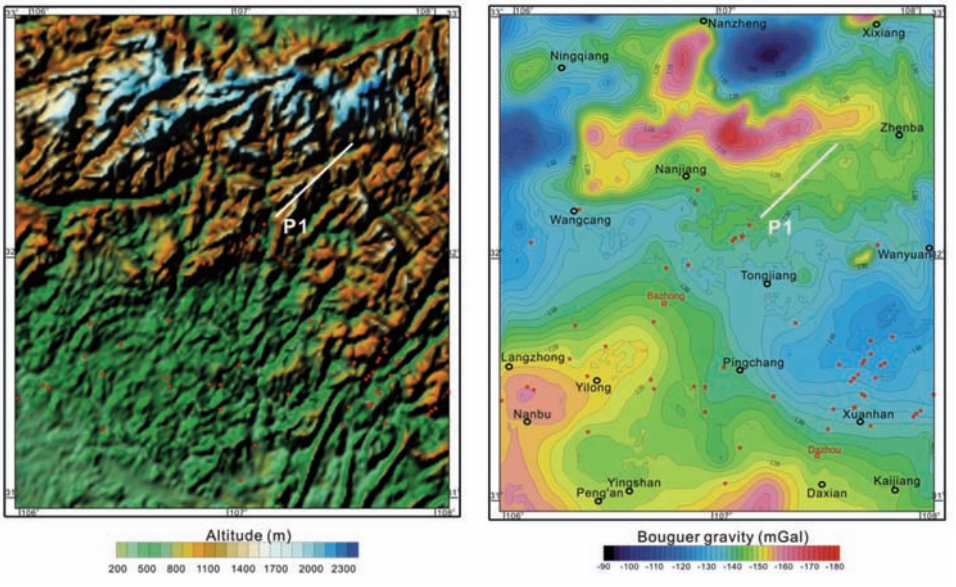

Fig. 2. (a) Topography and (b) 1:200,000 Bouguer gravity anomalies for the Micang structural zone and its adjacent area. The red stars represent the drill holes, and white lines indicate seismic reflection profiles. Topography is taken from the spherical harmonic model DTM2006.

JOINT INVERSION OF GRAVITY AND SEISMIC DATA

The term "cooperative inversion" of geophysical data, and particularly between seismic and gravity data, was defined by Lines et al. (1988). *They distinguished between* joint and sequential inversion. The sequential method treats the two data set separately (Vernant et al., 2002), whereas the joint one simultaneously places them into one data vector (Lees and VanDecar, 1991). Earlier cooperative inversions of Bouguer and seismic travel time data, either sequential or joint consider a constant linear relationship between density and velocity (e.g., Birch, 1961). However, in real cases, the correlation between velocity and density varies with depth, which can not be depicted by a constant. The approach we used here is based on the 2D generalized linear (iterative) inversion scheme (Backus and Gilbert, 1967), which simultaneously places the seismic travel time and gravity data into one data vector. In our method,

weighting matrices are incorporated into the joint objective function to evaluate the contribution of the two type of datasets. For the 2D layered model, an improved linear traveltime interpolation method (Zhang et al., 2009) is adopted for the travel time computation. The forward gravity modeling used in this study is based on the methods of Rasmussen and Pedersen (1979), in which a reasonable 2.5D model is constructed, using bodies of polygonal cross sections with finite extension length in the strike direction.

The inversion algorithm

The generalized linear inversion of the seismic reflection and Bouguer gravity data is accomplished by a least squares approach (Menke, 1989) on the joint objective function, in which different weighting matrices are incorporated on the two types of datasets.

Vector G stands for the observed gravity values, and S is the seismic traveltime vector. Vector G′ and S′ indicate the forward calculated gravity and traveltime values. The number of vector G and S is m_g and m_s, respectively. According to the principle of least squares, the joint inversion problem can be transformed into acquiring a model parameter vector $\bar{m} = (\bar{m}_g, \bar{m}_s)^T$, which minimize the $\|G - G^f\|^2$ and $\|S - S^f\|^2$. Therefore, the joint inversion scheme can be expressed as

$$W_G^2 \|G - G^f\|^2 + W_S^2 \|S - S^f\|^2 \leq \varepsilon \ , \tag{1}$$

where W_G and W_S are the relative weighting matrices on the gravity and seismic traveltime data. Starting from some initial model guess m^0, the above joint inversion problem can be linearized into an iterative scheme based on the generalized linear theory. The linear inversion problem can be expressed as

$$\begin{bmatrix} W_G A^G & 0 \\ 0 & W_S A^S \end{bmatrix} X = \begin{bmatrix} W_G B^G \\ W_S B^S \end{bmatrix} , \tag{2}$$

where X is the model modification vector, A^G and A^S are the partial derivative matrix of the model responses with respect to the model parameters. B^G and B^S are the gravity and seismic traveltime residual vectors between the observed and theoretical values.

Assuming our model has N interfaces, and the number of each interface is labeled as n_i ($i = 1, 2, \ldots, N$). m_d, m_ρ and m_v stand for the depth, density and velocity vector.

$$m_d = (Z_{11},Z_{12},\cdots,Z_{1n_1},Z_{21},\cdots,Z_{2n_2},\cdots,Z_{N1},Z_{N2},\cdots,Z_{Nn_N})^T \quad , \tag{3}$$

$$m_\rho = (\rho_1,\rho_2,\cdots,\rho_N)^T \quad , \tag{4}$$

$$m_v = (v_1,v_2,\cdots,v_N)^T \quad , \tag{5}$$

where Z_{ij} is the depth of the j-th node in the i-th layer. Then vector X in eq. (2) can be described as

$$x = (\Delta\rho_1,\Delta\rho_2,\cdots,\Delta\rho_N,\Delta Z_{11},\Delta Z_{12},\cdots,\Delta Z_{Nn_N},\Delta v_1,\Delta v_2,\cdots,\Delta v_N)^T \quad . \tag{6}$$

Therefore, the number of model parameter in the joint inversion is L (L = 2N + $\Sigma_{i=1}^{N} n_i$). The observed and theoretical traveltime S and S′ can be expressed as

$$S = (t_{11},t_{12},\cdots,t_{1n_1},t_{21},t_{22},\cdots,t_{2n_2},\cdots,t_{N1},t_{N2},\cdots,t_{Nn_N})^T \quad , \tag{7}$$

$$S^f = (t^f_{11},t^f_{12},\cdots,t^f_{1n_1},t^f_{21},t^f_{22},\cdots,t^f_{2n_2},\cdots,t^f_{N1},t^f_{N2},\cdots,t^f_{Nn_N})^T \quad . \tag{8}$$

The observed and theoretical gravity vector G and G′ are

$$G = (g_1,g_2,\cdots,g_{mg})^T \quad , \tag{9}$$

$$G^f = (g^f_1,g^f_2,\cdots,g^f_{mg})^T \quad . \tag{10}$$

Therefore, the residual vector between the observed and theoretical values for the gravity and seismic traveltime data are $B^G = G - G^f$ and $B^S = S - S^f$. The row and column numbers of the left matrix in eq. (2) are N_R and N_C, respectively, where

$$N_R = m_g + m_S = m_g + \sum_{i=1}^{N} m_i \quad , \tag{11}$$

$$N_C = 2(N + \sum_{i=1}^{N} n_i \quad . \tag{12}$$

The partial derivative matrices are

$$A_i^G = [(\partial g_i/\partial\sigma_1),(\partial g_i/\partial\sigma_2),\cdots,(\partial g_i/\partial\sigma_N),(\partial g_i/\partial Z_{11}),(\partial g_i/\partial Z_{12}),\cdots,$$

$$(\partial g_i/\partial Z_{1n_1}),(\partial g_i/\partial Z_{21}),(\partial g_i/\partial Z_{22}),\cdots,(\partial g_i/\partial Z_{2n_2}),\cdots,(\partial g_i/\partial Z_{N1}),$$

$$(\partial g_i/\partial Z_{N2}),\cdots,(\partial g_i/\partial Z_{Nn_N}) \quad , \quad i = 1,2,\cdots,m_g. \tag{13}$$

$$A_{ij}^{S} = [(\partial t_{ij}/\partial Z_{11}),(\partial t_{ij}/\partial Z_{12}),\cdots,(\partial t_{ij}/\partial Z_{1n_1}),(\partial t_{ij}/\partial Z_{21}),(\partial t_{ij}/\partial Z_{22}),\cdots,$$

$$(\partial t_{ij}/\partial Z_{2n_2}),\cdots,(\partial t_{ij}/\partial Z_{N1}),(\partial t_{ij}/\partial Z_{N2}),\cdots,(\partial t_{ij}/\partial Z_{Nn_N}),(\partial t_{ij}/\partial v_1),$$

$$(\partial t_{ij}/\partial v_2),\cdots,(\partial t_{ij}/\partial v_N) \quad , \quad i = 1,2,\cdots,N, \quad j = 1,2,\cdots,m_i. \tag{14}$$

There is always part of the elements in A^S are zero, due to the limited ray coverage of the reflected seismic waves. After setting up the initial model estimations, we can conduct the iterative linear inversion with the least squares approach (Fig. 3).

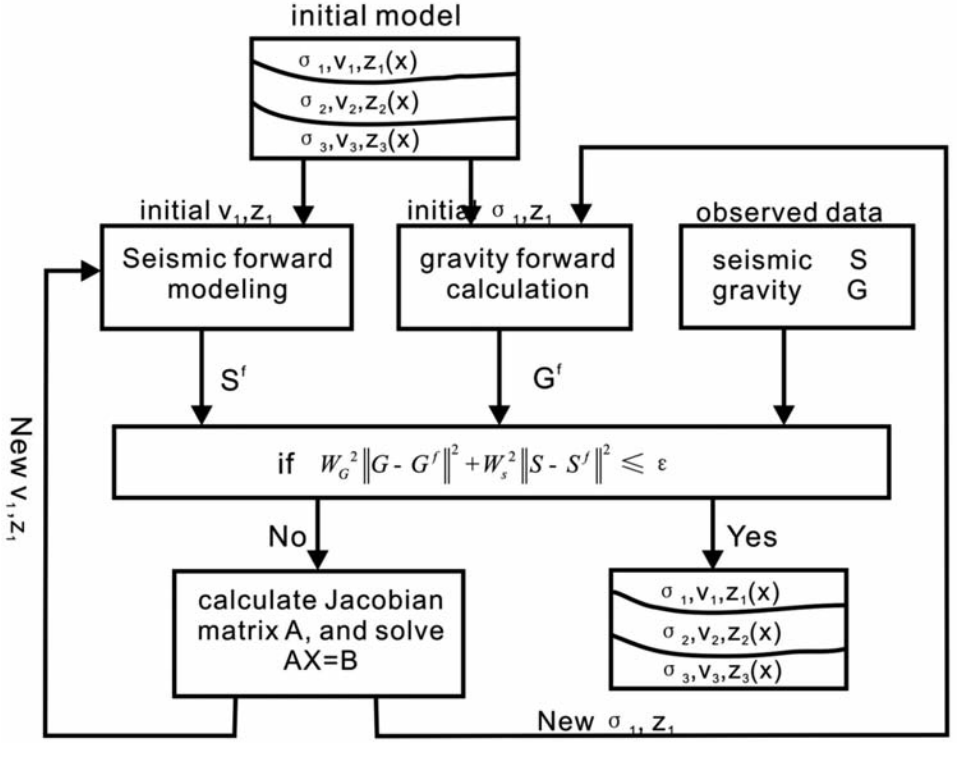

Fig. 3. Flowchart of the joint inversion procedure. The Jacobian matrix A refers to the one in the left bracket, and B is the residual matrix in the right bracket in eq. (2). ε is prescribed tolerance of the misfit between the theoretical and observed data (see text for detailed explanation).

Initial model estimation

The solution of our iterative linear inversion problem more or less depends on the starting model. In the joint inversion of gravity and seismic data, the seismic traveltime is usually derived from the stacked reflection sections, which relies greatly on the estimation of velocity and depth. For the ground gravity data, it also has strong dependence on the depth and density contrast. Therefore, the initial starting model is of great significance for the joint inversion results.

For the real cases, the starting model is preferably chosen from the drilling data. By comparing the traveltime traces of the reflected waves in the stacked sections with their corresponding reflectance in the drill hole profiles, we can determine the initial layer depths. The zero-offset vertical seismic profile (VSP) is a good tool to provide us the seismic wave velocities, and the borehole gravity measurement (BHGM) can offer more accurate density estimations. If no VSP or BHGM documents available, we can use the acoustic logging and density logging data as alternatives. For example, when determining velocities from the acoustic logging data, we need first to divide the continuous acoustic logging curves into segments, according to the stratigraphic column and stacked time section. Then the interval velocity can be calculated from the layer thickness Δh_i and travel time ΔT_i ($v_i = \Delta h_i/\Delta T_i$).

Regularization

The inversion will typically be ill-posed, and as such will require regularization. The regularization in our paper is adopted both on the model parameters and the data. The regularization on the model parameters is implemented by dividing the elements of each column in the Jacobian matrix A with the square root of the sum of their squares.

If the data is statistically independent, we can use the standard deviation to regularize the data to be dimensionless. Let σ_i^G, $i = 1,2,\cdots,m_s$ and σ_{li}^S, $i = 1,2,\cdots,m_l$; $l = 1,2,\cdots,L$ be the standard deviation of gravity and seismic travel time data, the weighting matrices in eq. (1) can be transformed into

$$W_G = \begin{bmatrix} 1/\sigma_1^G & & & 0 \\ & 1/\sigma_2^G & & \\ & & \diagdown & \\ 0 & & & 1/\sigma_{mG}^G \end{bmatrix}, \tag{15}$$

$$W_S = \begin{bmatrix} 1/\sigma_{l1}^S & & & & & & 0 \\ & \backslash & & & & & \\ & & 1/\sigma_{lm_l}^S & & & & \\ & & & \backslash & & & \\ & & & & 1/\sigma_{L_1}^2 & & \\ & & & & & \backslash & \\ 0 & & & & & & 1/\sigma_{Lm_L}^2 \end{bmatrix}, \quad (16)$$

where the elements of the diagonal weighting matrices are the reciprocal of standard deviations.

If the standard deviations of the observed data are unknown, we can apply the regularization scheme based on the criterion of the relative root mean square error. In this sense, the weighting matrices W_G and W_S can be expressed as

$$W_G = \frac{1}{\sqrt{m_G}} \begin{bmatrix} 1/g_1^D & & & 0 \\ & 1/g_2^D & & \\ & & \backslash & \\ 0 & & & 1/g_{m_G}^D \end{bmatrix}, \quad (17)$$

$$W_S = \frac{1}{\sqrt{m_S}} \begin{bmatrix} 1/t_{l1}^D & & & & & & 0 \\ & \backslash & & & & & \\ & & 1/t_{lm_l}^D & & & & \\ & & & \backslash & & & \\ & & & & 1/t_{L1}^D & & \\ & & & & & \backslash & \\ 0 & & & & & & 1/t_{Lm_L}^D \end{bmatrix}, \quad (18)$$

whose diagonal elements are the reciprocal of the observed values.

However, the inversion results are not only affected by the nature of geophysical data, such as values, accuracy, and number of data points, but also depends on some subjective factors, like the sensitivity of the model response to its modifications. Therefore, we introduced a weighting factor W on the weighting matrix W_S to evaluate the contributions coming from these two different datasets. With respect to the interface depth variations, the seismic traveltime is usually more sensitive than the ground gravity anomalies. Hence, a weighting factor larger than 1 is multiplied with W_S to strengthen the seismic part. If we use the non-zero offset seismic reflection traveltime data, the weighting factor should be larger than that using the zero-offset data. It is noteworthy that if we assign larger weighting factor on the seismic data, smaller traveltime residuals should be satisfied. Actually, it is a difficult task to evaluate the contributions of these two datasets accurately, and the weighting factor can only be estimated empirically.

Synthetic model

To test this method, we used a synthetic example consisting of five layers, each with different density and P-wave velocity (Fig. 4a). The model density and velocity are kept constant for each layer. We then estimate the velocity, density and depths for a layer-cake earth model from the joint inversion of zero-offset seismic reflection and Bouguer gravity data. We computed the zero-offset seismic traveltime (Fig. 4b) from an improved linear traveltime interpolation method (Zhang et al., 2009). Fig. 4c shows the calculated Bouguer gravity anomaly of the layer-cake earth model in Fig. 4a.

Fig. 5 shows the initial model for waveform inversion. For the weighting functions, we chose W_S:W_G = 2:1 for the common assumption that the seismic data have a higher resolution and S/N ratio than the gravity data.We continued inversion up to 10 iterations to converge to solution. Joint inversion of seismic and gravity data resolved the density and velocity structure well (Fig. 5, Table 1). For the multi-layered model, the joint inversion has better results for the upper layers than the lower ones, due to the rapid decrease of the gravity anomaly as a function of depth. Therefore, a weighting factor (W = 2) is added on the seismic data. As indicated in Table 1, the estimation of density contrast has also been benefited from the incorporation of seismic data in the joint inversion for helping better defining the interface depths.

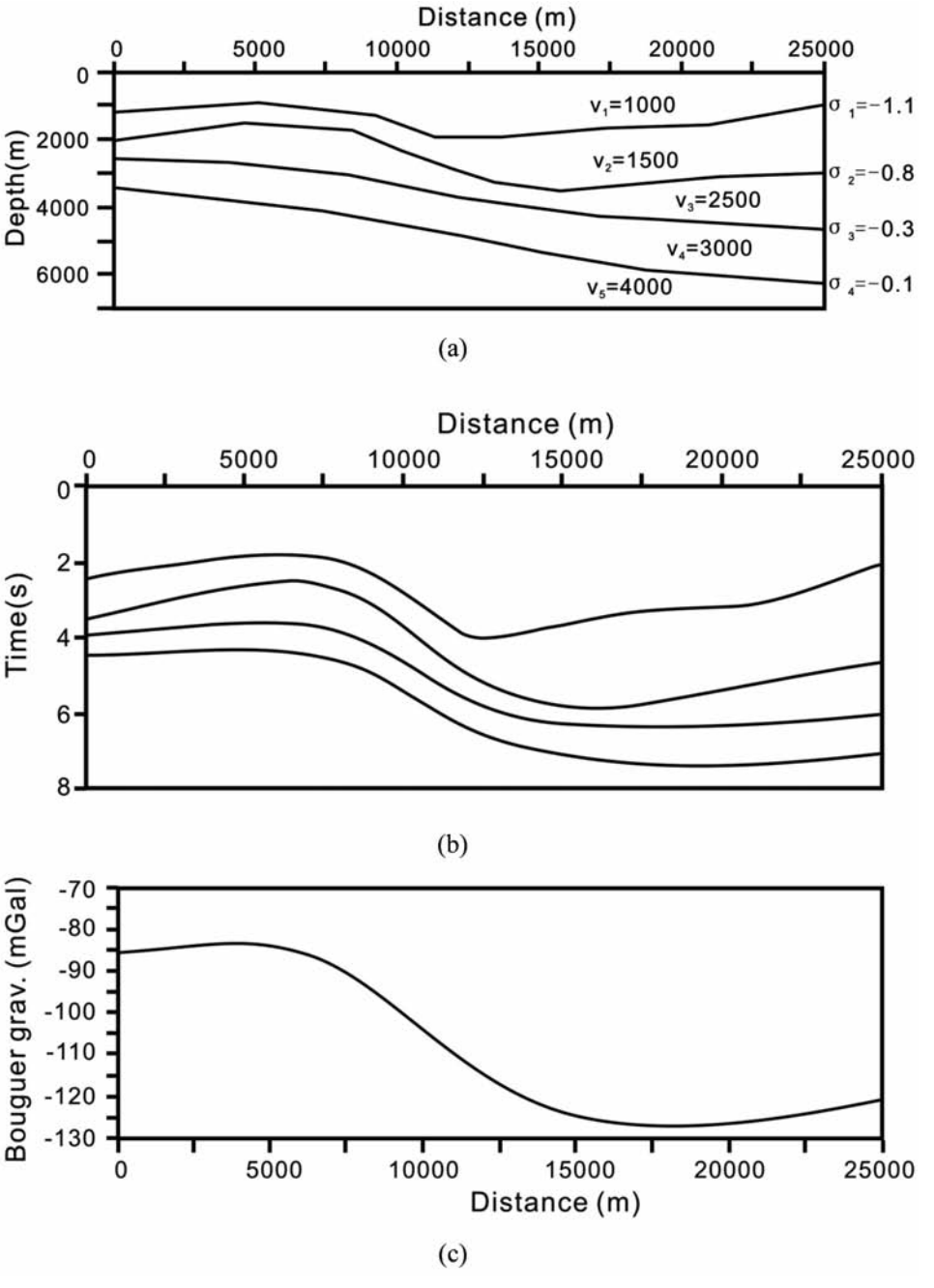

Fig. 4. The synthetic model. (a) Layer-cake earth model used as a true model to generate the synthetic seismic traveltime and gravity data. Units for velocity and density are: m/s and g/cm^3; (b) Zero-offset seismic reflection traveltime of the model in (a); (c) Bouguer gravity anomaly of the layer-cake earth model.

Table 1. Joint inversion results for the layer-cake earth model and comparison with the true model.

	Nodes	True depth	Initial depth	Joint inverted depth	Depth residuals	Velocity residuals	Density residuals
1st layer	0.0	1182.3	1182.3	1172.670	9.630	8.806	0.00812
	5120.0	921.9	1208.3	914.233	7.667		
	9210.0	1286.5	1442.7	1275.010	11.490		
	11330.0	1911.5	1572.9	1894.350	17.150		
	13550.0	1937.5	1677.1	1921.000	16.500		
	17330.0	1651.0	1807.3	1637.150	13.850		
	20950.0	1546.9	1807.3	1533.870	13.030		
	24750.0	1052.1	1781.3	1043.130	8.970		
2nd layer	0.0	2015.6	1807.3	2010.18	5.420	8.540	0.00377
	4570.0	1520.8	1911.5	1516.13	4.670		
	8440.0	1729.2	2302.1	1723.09	6.110		
	10060.0	2328.1	2484.4	2315.55	12.550		
	11800.0	2849.0	2692.7	2838.95	10.050		
	13380.0	3239.6	2901.0	3234.30	5.300		
	15760.0	3526.0	3057.3	3522.85	3.150		
	21290.0	3109.4	3239.6	3107.72	1.680		
	24750.0	2979.2	3187.5	2981.75	-2.550		
3rd layer	0.0	2588.5	2458.3	2618.64	-30.140	173.52	0.01065
	4060.0	2692.7	2875.0	2756.81	-64.110		
	8310.0	3057.3	3265.6	3133.26	-75.960		
	11970.0	3682.3	3682.3	3715.70	-33.400		
	17120.0	4255.2	4020.8	4301.16	-45.960		
	24750.0	4645.8	4411.5	4752.94	-107.140		
4th layer	0.0	3421.9	4489.6	3463.11	-41.21	101.09	-0.00346
	7380.0	4125.0	4750.0	4218.69	-93.690		
	12360.0	4880.2	4984.4	4926.66	-46.46		
	15380.0	5401.0	5140.6	5453.94	-52.940		
	18780.0	5895.8	5375.0	5977.86	-82.060		
	24750.0	6234.4	5739.6	6361.17	-126.770		
Units: depth (m); density (g/cm^3); velocity (m/s)							

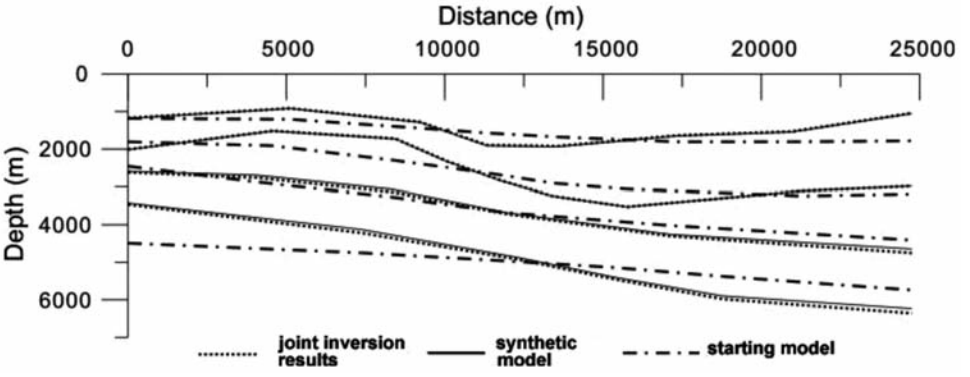

Fig. 5. Estimated model from the joint inversion of zero-offset seismic reflection data and gravity data.

APPLICATIONS TO THE MICANG FORELAND BELT

The joint inversion method was applied to seismic and gravity data of profile P1 in order to investigate the shallow structure of the Micang foreland belt. The southern part of profile P1 crosses the margin of Sichuan Basin, whose seismic reflection image is clear with obvious indications on main reflectance. But for its northern part in the foreland of the Micang anticlinorum, the seismic reflection data is in poor quality due to complicated geological structures in the leading edge of the Micang Mountains. The seismic reflection image at the Micang foreland belt is ambiguous, causing difficulty in tracing the reflection horizon. As indicated in Fig. 6, the reflection time section derived from the time migration data do not have adequate information in its northern part to derive a reliable structure of the Micang foreland belt. The contribution of gravity data allows better constraining the morphology of the missing part, where the seismic resolution is poor or absent.

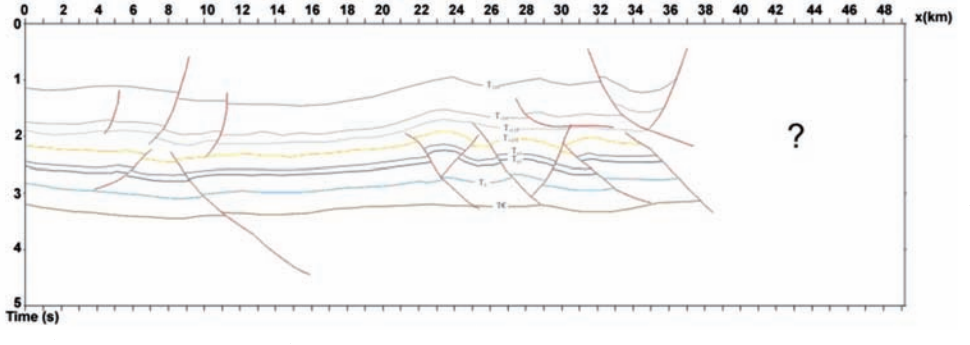

Fig. 6. The seismic structural model from the reflection time migration section of profile P1.

Initial starting model

For establishing the initial density and velocity model, we need to convert the two-way traveltime (TWT) to depth by using velocities of the strata (Li, 1992). Fig. 7 indicates the relationship between the two-way traveltime (TWT) versus depth, derived from the available drilling data near profile P1. The depth profile converted from the time section is shown in Fig. 8, whose depths are adopted as the initial estimation of our layer model (Fig. 9). For the north part of the profile P1, where the seismic data is missing, we assumed its initial model consists of six horizontal layers. The density contrasts and velocities for each layer are inferred from previous drilling data and rock sample measurements (Zhou et al., 1992). The density contrasts for the Jurassic, Triassic, Permian, Silurian and Cambrian strata with respect to the underlying Sinian stratum are -0.15, -0.12, -0.09, -0.04 and -0.02 g/cm^3. The velocities for each layer from top the bottom are 4750, 5400, 6000, 6500, and 7000 m/s.

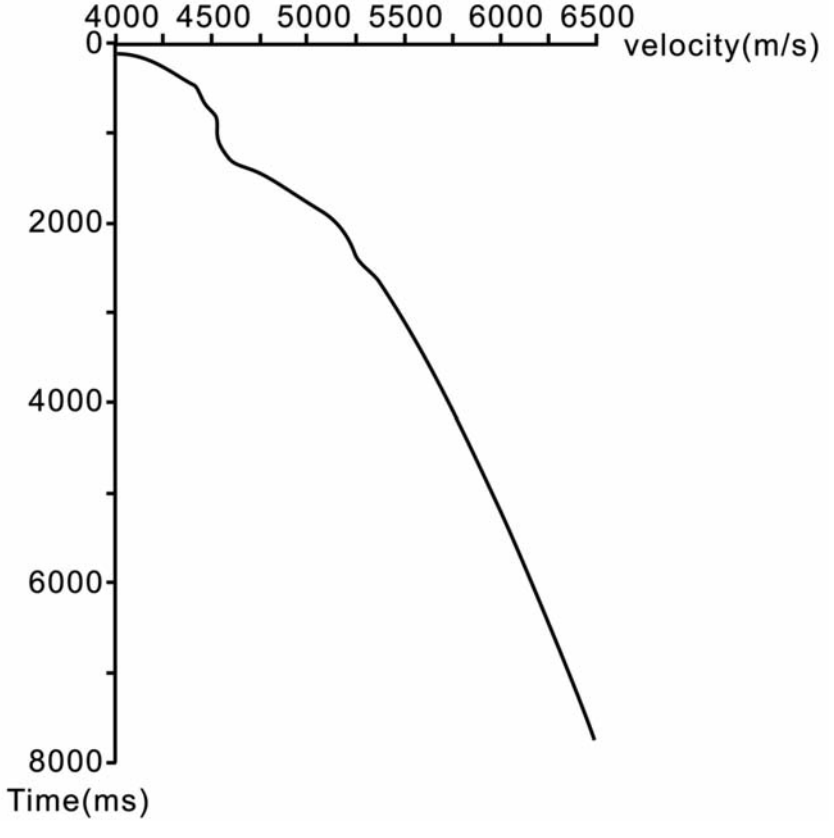

Fig. 7. Two-way traveltime (TWT) versus depth for profile P1.

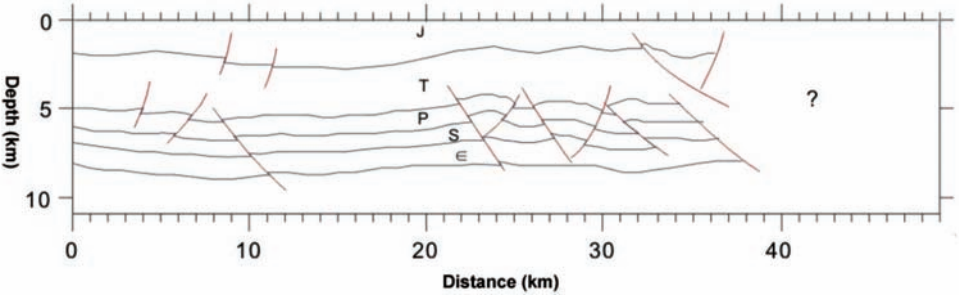

Fig. 8. The seismic depth section of profile P1 converted from the time section in Fig. 6.

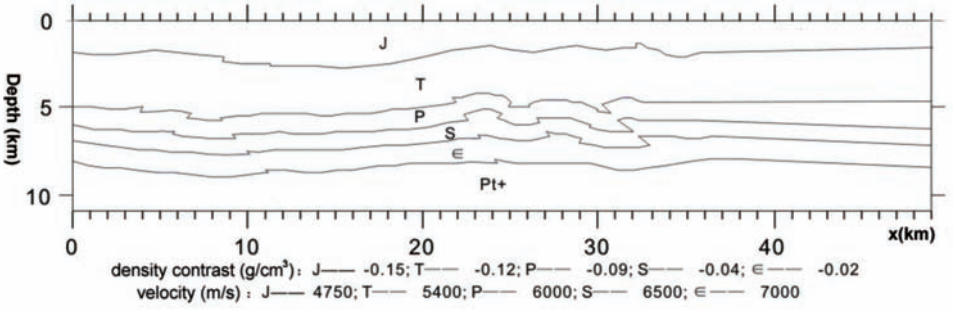

Fig. 9. Starting model for the joint inversion of seismic reflection traveltime and gravity data. The density contrasts and velocities for each layer are indicated at the bottom.

Gravity field separation

To separate the gravity field of the folded basement and its overlying layers from the observed gravity data, we need to remove the gravity effects of the Moho topography. The wavelet multi-resolution analysis is then adopted for the gravity field separation. The third-order wavelet approximations (red dashed line in Fig. 10) are assumed to be the reflection of the gravity field caused by the Moho undulations. While the third-order wavelet details (blue line in Fig. 10) are taken as the residual gravity field generated by the folded basement and its overlying strata, which are the gravity data input for the joint inversion.

Joint inversion of seismic and gravity data

Due to the better resolution of seismic inversion than the gravity inversion, we assigned a weighting factor (W = 3) on the seismic data, after the

regularization of these two datasets. Also the more reliable solution in the southern part of our profile can be used as constraints to invert the northern part in the Micang foreland belt. After 10 iterations, the joint inversion results are shown in Fig. 11b. Fig. 11a indicates the misfit between the theoretical and observed data. The inverted densities and velocities for each layer are indicated at the bottom of Fig. 11, which in line with the statistics of rock sample measurements and drilling data (Zhou et al., 1992).

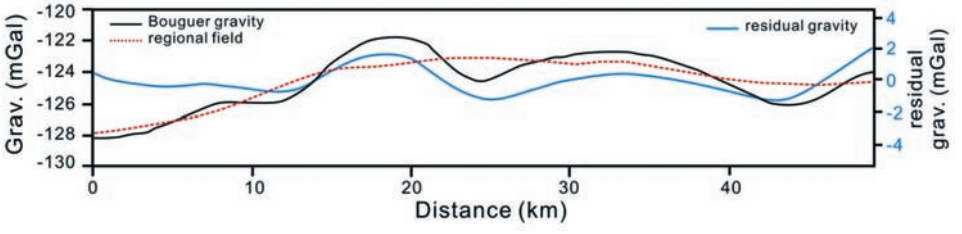

Fig. 10. Bouguer gravity (black line), regional (red dashed) and local gravity field (blue line) derived from the wavelet multi-resolution analysis.

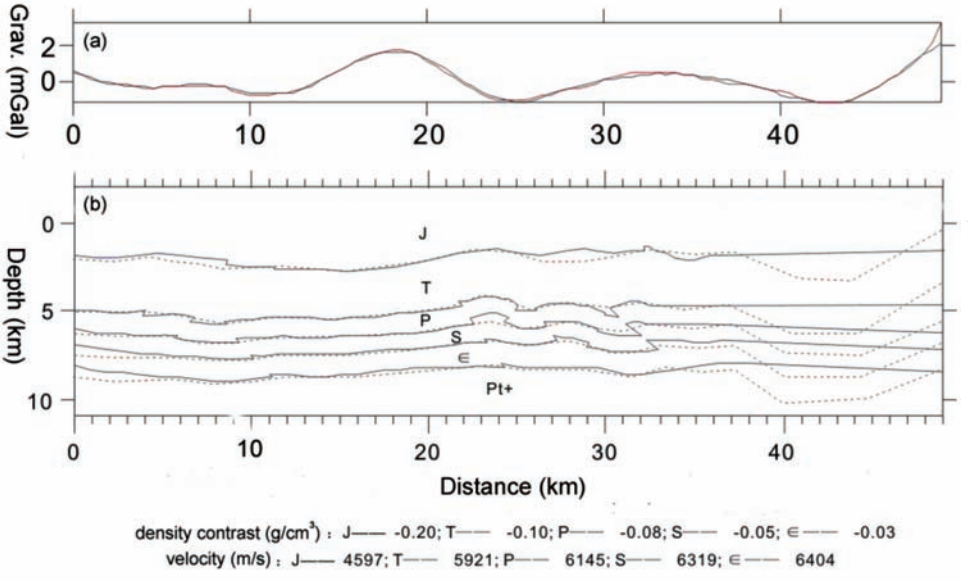

Fig. 11. Joint inversion results of profile P1. (a) Misfit between the observed and calculated gravity data from the final layered model, blue and red lines are the observed and theoretical gravity respectively; (b) The comparatione of the final inverted model (dashed lines) with the initial starting model (solid lines).

DISCUSSION AND CONCLUSIONS

The inherent ambiguity in geophysical interpretation can always lead us to a completely unrealistic model by showing an excellent agreement between observed and computed data. Combined use of several different geophysical datasets can help us in constraining the model, especially when the seismic data is in poor quality or absent. In the present work we have applied a weighted least-squares analysis to a joint inversion in geophysics that links seismic reflection traveltime and ground gravity data together. After being testified by a layer-cake earth model, it was used to image the upper crustal structure of the Micang foreland belt. The initial depth model was constructed mainly from the seismic time migration section. But for the northern part beneath the Micang foreland belt, where the seismic data is not available, the initial layer model was assumed to be horizons. Then the joint inversion of travel time and gravity data is performed to find out a common model having an optimum fit of both travel time and gravity data.

As indicated in Fig. 11, the joint inversion results at the southern part of the profile P1 (distance: 0 - 30 km) consistent well with the initial model derived from the seismic time migration section. But for the northern part, there is a gravity low at the distance of 40 - 45 km, which could be reflection of a rift. While the gravity rise at the north end (distance: 45 - 49 km), perhaps represents the basement uplift at the Micang foreland belt. Therefore, the gravity data inversion for the northern part of profile P1, where the seismic data is absent, can be used to better constrain the geological structures beneath the Micang foreland belt.

Finally we try to infer the geological structures of the whole profile by incorporating the joint inversion results in Fig. 11, and comparing it with the seismic time migration section (Fig. 8). The time migration section we finally deduced is shown in Fig. 12a. With the TWT-depth relationship (Fig. 7), we can get a more complete geological structures of the whole profile P1 (Fig. 12b).

The Micang structural zone, Longmenshan intra-continental orogen and the Daba foreland faulted thrust belt are all located at the north margin of the Yangtze plate. Compared with the other two structures, the Micang structural zone is more distant from the plate margin. During the closure of the Paleo-Tethys Southern Qinling Ocean, the northward bulged Hannan igneous complex collided with the Qinling micro-plate, forming strong strike-slip effects and lateral extrusion along the both sides of the Hannan igneous complex. According to the magnetotelluric sounding results (Cheng et al., 2003), the Yangtze plate subducted northwardly to the Qinling orogen at the depth of about 40 km. Therefore, at the tectonic background of NS compression, the overthrust from north to south can be witnessed in the Micang foreland belt (Fig. 12b, c).

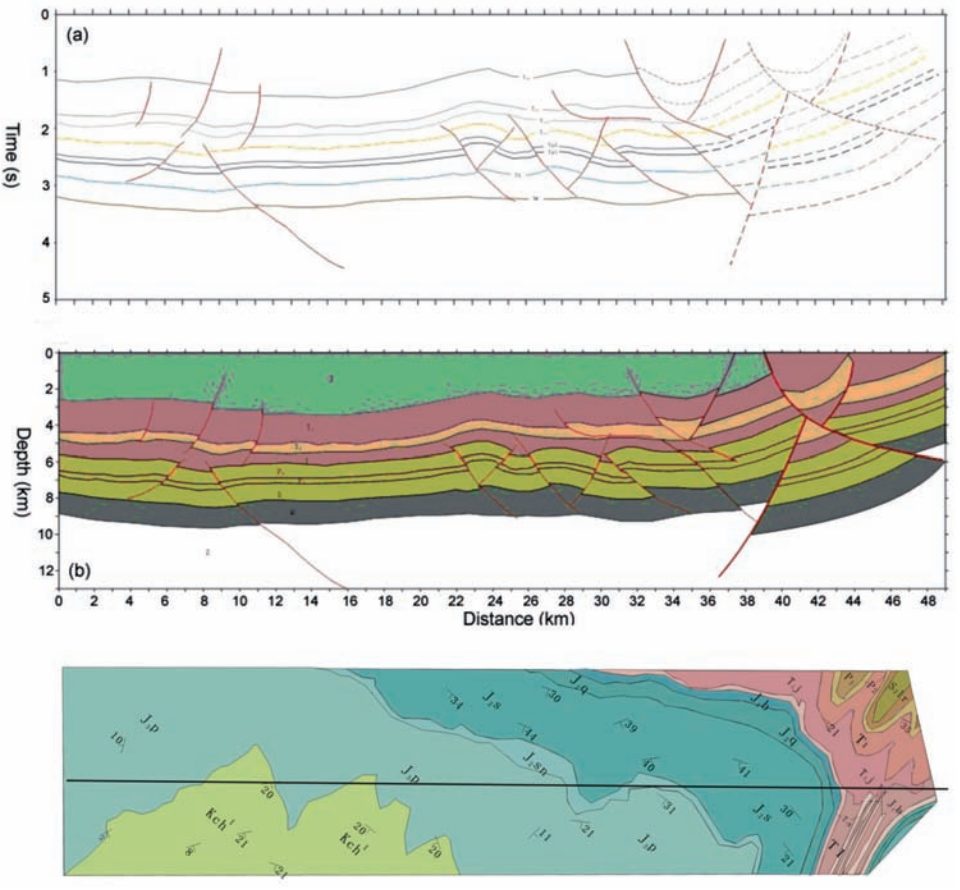

Fig. 12. (a) The seismic time migration section inferred from the joint inversion results; (b) The final geological section of profile P1; (c) surface geology along profile P1 and its adjacent area. The dashed lines indicating the structures underneath the Micang foreland belt, which are deduced from the joint inversion results in Fig. 11.

ACKNOWLEDGEMENTS

This study was supported by the National Science Foundation of China (No. 41104081, No. 41204064), and the Special Fund for Basic Scientific Research of Central Colleges, China University of Geosciences, Wuhan) (No. CUG090106 and No.CUGL100205). We are also grateful to the Editor and the anonymous reviewers for their constructive comments and suggestions, which will significantly improve the manuscript.

REFERENCES

Aki, K., Christofferson, A. and Husebye, E., 1977. Determination of the three-dimensional seismic structure. J. Geophys. Res., 82: 277-296.

Birch, F., 1961. The velocity of compressional waves in rocks to 10 kilobars. J. Geophys. Res., 66: 2199-2224.

Buckus., G.E. and Gilbert., J.F., 1967. Numerical application of a formalism for geophysical inverse problems. Geophys. J., 13: 247-276.

Cheng, S.Y., Zhang, G.W. and Li, L, 2003. Lithospheric electrical structure of the Qinling orogen and its geodynamic implication. Chin. J. Geophys., 46: 556-567.

Clark, M. and Royden, L., 2000. Topographic ooze: Building the eastern margin of Tibet by lower crustal flow. Geology, 28: 703-706.

Deng, B., Liu, S.G., Li, Z.W., Liu, S., Wang, G.Z. and Li, G.Z., 2008. A comparative study of the late Mesozoic uplifting in the eastern margin of Qinghai-Tibet Plateau and Sichuan Basin, China. J. Chengdu Univ. Technol. (Science Technol. Ed.), 35: 477-486.

Dong,Y.P., Zhang, G.W., Neubauer, F., Liu, X.M., Genserb, J. and Hauzenberger, C., 2011. Evolution of the Qinling orogen, China: Review and synthesis. J. Asian Earth Sci., 41: 213-237.

Enkelmann, E., Ratschbacher, L., Jonckheere, R., Nestler, R., Fleischer, M., Gloaguen, R., Hacker, B.R., Zhang, Y.Q. and Ma, Y.S., 2006. Cenozoic exhumation and deformation of northeastern Tibet and the Qinling: Is Tibetan lower crustal flow diverging around the Sichuan Basin? Geol. Soc. Am. Bull., 118: 651-671.

Gao. S, Zhang, B.R., Li, Z.J., Wang, D.P., Ouyang, J.P. and Xie, Q.L., 1996. Geochemical evidence for the Proterozoic tectonic evolution of the Qinling orogenic and its adjacent margins of the North China and Yangtze Cratons. Precambr. Res., 80: 23-48.

Harris, N., 2007. Channel flow and the Himalayan-Tibetan orogen: a critical review. J. Geol. Soc. London, 164: 511-523.

Jess, K., Nigel, H., Tom, A., Randy, P., Bruce, C., Sarah, S. and Zhang, H.F., 2007. First field evidence of southward ductile flow of Asian crust beneath southern Tibet. Geology, 35: 727-730.

Julia, J., Ammon, C., Herrmann, R. and Correig, A., 2000. Joint inversion of receiver function and surface wave dispersion observations. Geophys. J. Internat., 143: 99-112.

Lees, J. and VanDecar, J., 1991. Seismic tomography constrained by Bouguer gravity anomalies: Applications in Western Washington. Pure Appl. Geophys., 135: 31-52.

Lee, J. and Whitehouse, M., 2007. Onset of middle crustal ductile flow in southern Tibet: evidence from U/Pb zircon ages. Geology, 35: 45-48.

Li, X., 1992. The joint inversion of seismic and gravity data- different ways of implementation. Nat. Gas Geosci., 5: 37-42.

Li, Z.W., 2006. The Formation and Evolution of the Daba Thrust Belts and its Foreland Basins in the Mesozoic-Cenozoic Period. Ph.D. Thesis, Chengdu University of Technology, Chengdu.

Lines, L., Schultz, A. and Treitel, S., 1988. Cooperative inversion of geophysical data. Geophysics, 53: 8-20.

Liu, S.F., Zhang, G.W. and Dai, S.W., 2001. Evolution of Qinling Mianlue Belt: Evidence from Sedimentology and Tectonics of the Northern Yangtze, China. Gondw. Res., 14: 690-691.

Liu, S., 2007. Structural Characteristics of the Thrust Fold of Foreland. Ph.D. Thesis, Institute of Geology, China Earthquake Administration, Beijing.

Liu, S.G., 1993. The formation and evolution of the Longmenshan thrust belt and the foreland basins in the western Sichuan. Publishing House, Chengdu Univ. of Technology, Chengdu.

Liu, S.G., Li, Z.W. and Cao, J.X., 2009. The four-dimensional structure of the Longmenshan composite orogen. Chin. J. Geol., 44: 1151-1180 (In Chinese with English abstract).

Liu, S.G., Li, Z.W., Liu, S., Luo, Y.H., Xu, G.Q., Dai, G.H., Gong, C.M. and Yong, Z.Q., 2006. The formation and evolution of the Daba thrust belts and its foreland basins. Geological Publishing House, Beijing.

Lin Y.F., Zeng, X.P. and Guo, Q.H., 1985. Analysis of secular variations of non-dipole geomagnetic-field in east-Asia. Acta Geophys. Sinica, 28: 482-496.

Maceira, M. and Ammon, C., 2009. Joint inversion of surface wave velocity and gravity observations and its application to central Asian basins shear velocity structure. J. Geophys. Res., 114: B02314.

McClay, K.R. (Ed.), 1992. Trust Tectonics. Chapman and Hall, London.

Meng, Q.R. and Zhang, G.W., 1999. Timing of collision of the North and South China blocks: Controversy and reconciliation. Geology, 27: 123-126.

Meng, Q.R. and Zhang, G.W., 2000. Geologic framework and tectonic evolution of the Qinling orogen, Central China. Tectonophys., 323: 183-196.

Menke, W., 1989. Geophysical Data Analysis: Discrete Inverse Theory. Academic Press Inc., San Diego.

Parsons, T., Blakely, R. and Brocher, T., 2001. A simple algorithm for sequentially incorporating gravity observations in seismic traveltime tomography. Internat. Geol. Rev., 43: 1073-1086.

Coward, M.P., Deramond, J., Hossack, J. and Platt, J.P. (Eds.), 1986. Internat. Conf. Thrusting and Deformation. J. Struct. Geol., 8: 215-483.

Rasmussen, R. and Pedersen, L.B., 1979. End corrections in potential field modeling. Geophys. Prosp., 27: 749-760.

Sun, D., 2011. The structural character and Meso-Cenozoic evolution of Micang Mountain Structural Zone, Northern Sichuan Basin , China. Ph.D. Thesis, Chengdu Univ. of Technology, Chengdu.

Sun, Y., Lu, X.X., Han, S. and Zhang, G.W., 1996. Composition and formation of Paleozoic Erlangping ophiolitic slab, North Qinling: evidence from geology and geochemistry. Sci. Sinica, 39: 50-59.

Tikhotsky, S. and Achauer, U., 2008. Inversion of controlled-source seismic tomography and gravity data with the self-adaptative wavelet parametrization of velocities and interfaces. Geophys. J. Internat., 172, 619-630.

Vernant, P., Masson, F., Bayer, R. and Paul, A., 2002. Sequential inversion of local earthquake traveltimes and gravity anomaly - The example of the Western Alps, Geophys. J. Int. 150: 79-90.

Zhang, D., Xie, B.L., Yang, Y., Fu, X.R. and Qin, Q.Q., 2009. A ray tracing method based on improved linear traveltime interpolation. Chin. J. Geophys., 52: 200-205 (in Chinese with English abstracts).

Zhang, G.W., Cheng, S.Y., Guo, A.L., Dong, Y.P, Lai, S.Z. and Yao, A.P., 2004. Mianlue paleo-suture on the southern margin of the Central Orogenic System in Qinling-Dabie with a discussion of the assembly of the main part of the continent of China. Geol. Bull. China, 23: 846-853 (in Chinese with English abstract).

Zhang, K.J., 1997. North and South China collision along the eastern and southern North China margin. Tectonophys., 270: 145-156.

Zhao, X.X. and Coe, R.S., 1987. Paleomagnetic constraints on the collision and rotation of North and South China. Nature, 327: 141-144.

Zhou, G.F., Luo, X.K. and Guan, Z.N., 1992. Research on relationship between characteristics of geophysical field and crustal architecture and deep structure in the Qinling-Daba Mts. China Univ. of Geosciences Press Co. Ltd., Wuhan.

APPENDIX

Partial derivative elements in the Jacobian matrix A

1. Partial derivative of traveltime with respect to the velocity and depth

For the l-th interface, the partial derivative of the reflection traveltime t versus the velocity v_l is

$$\partial t/\partial v_l = -2\cdot d_{l(l-1)}/v_l^2 \quad . \tag{A-1}$$

Assuming the reflectance segment between nodes (x_{li}, z_{li}) and $(x_{l(i+1)}, z_{l(i+1)})$ is a straight line, we can get

$$\begin{aligned} \partial t/\partial z_{li} &= (\partial t/\partial z_{Rl})\cdot(\partial z_{Rl}/\partial z_{li}) = P\cdot Q \quad , \\ \partial t/\partial z_{l(i+1)} &= (1 - P)\cdot Q \quad , \end{aligned} \tag{A-2}$$

where

$$P = 1 - (x_{Ri} - x_{li})/(x_{l(i+1)} - x_{li}) \quad ,$$

$$Q = 2\cdot(z_{Rl} - z_{R(l-1)})/v_l\cdot d_{l(l-1)}) \quad .$$

2. Partial derivative of gravity anomaly with respect to the density and depth

In the 2.5D sense, the partial derivatives of the gravity anomaly versus the density and depth are accomplished using the difference instead of differential.

$$\partial(\Delta g)/\partial z_j = G\cdot\sigma \sum [-2\sin\varphi_i(\partial \subset_i/\partial z_j)F(i) + 2\cos\varphi_i(\partial F_i/\partial z_j)] \quad , \tag{A-3}$$

$$\partial \subset_i/\partial z_j = \begin{cases} (x_{i+1} - x_i)/[(x_{i+1} - x_i)^2 + (z_{i+1} - z_i)^2] & , j = i \\ (-x_{i+1} + x_i)/[(x_{i+1} - x_i)^2 + (z_{i+1} - z_i)^2] & , j = i+1 \\ 0 & , \text{others} \end{cases} \tag{A-4}$$

$$\begin{aligned} \partial F(i)/\partial z_j = {} & L\cdot[(u_i+R_i)/(u_{i+1}+R_{i+1})] \\ & \cdot[A2/(u_i+R_i) + A7/(u_i+R_i) - (u_{i+1}+R_{i+1})(A1+A6)/(u_i + R_i)^2] \\ & - A3[tg^{-1}(u_{i+1}\cdot L/w_i\cdot R_{i+1}) - tg^{-1}(u_i\cdot L/w_i\cdot R_i)] \end{aligned}$$

$$+ A2\cdot\ln[(L+R_{i+1})/r_{i+1}] + u_{i+1}\cdot\{[r_{i+1}\cdot A7 - (R_{i+1}+L)\cdot A5]/(L+R_{i+1})\}$$

$$- w_i\cdot\{[w_iR_{i+1}L\cdot A2 - R_{i+1}u_{i+1}L\cdot A3 - w_iu_{i+1}L\cdot A7]/[(w_iR_{i+1})^2+(u_{i+1}L)^2]$$

$$- [w_iR_iL\cdot A1 - R_iu_iL\cdot A3 - w_iu_iL\cdot A6]/[(w_iR_i)^2+(u_iL)^2]\}$$

$$- A1\cdot\ln[(L+R_i)/r_i] - u_i\cdot\{[r_i\cdot A6 - (R_i+L)\cdot A4]/(L+R_i)\} \quad , \qquad \text{(A-5)}$$

$$A1 = \partial u_i/\partial z_j = \begin{cases} (-x_i\sin\phi_i+\sin\phi_i+z_i\cos\phi_i)(x_{i+1}-x_i)/[(x_{i+1}-x_i)^2+(z_{i+1}-z_i)^2], & j=i \\ (-x_i\sin\phi_i+z_i\cos\phi_i)(x_i-x_{i+1})/[(x_{i+1}-x_i)^2+(z_{i+1}-z_i)^2], & j=i+1 \\ 0 \quad , \text{ others} \end{cases} \qquad \text{(A-6)}$$

$$A2 = \partial u_{i+1}/\partial z_j = \begin{cases} (-x_{i+1}\sin\phi_i+z_{i+1}\cos\phi_i)(x_{i+1}-x_i)/[(x_{i+1}-x_i)^2+(z_{i+1}-z_i)^2], & j=i \\ (-x_{i+1}\sin\phi_i+z_{i+1}\cos\phi_i)(x_i-x_{i+1})/[(x_{i+1}-x_i)^2+(z_{i+1}-z_i)^2]+\sin\phi_i, & j=i+1 \\ 0 \quad , \text{ others} \end{cases} \qquad \text{(A-7)}$$

$$A3 = \partial w_i/\partial z_j = \begin{cases} (-x_i\cos\phi_i-z_i\sin\phi_i)(x_{i+1}-x_i)/[(x_{i+1}-x_i)^2+(z_{i+1}-z_i)^2]+\cos\phi_i, & j=i \\ (-x_i\cos\phi_i-z_i\sin\phi_i)(x_i-x_{i+1})/[(x_{i+1}-x_i)^2+(z_{i+1}-z_i)^2], & j=i+1 \\ 0 \quad , \text{ others} \end{cases} \qquad \text{(A-8)}$$

$$A4 = \partial r_i/\partial z_j = (u_i\cdot A1 + w_i\cdot A3)/(u_i^2 + w_i^2)^{1/2} \quad , \qquad \text{(A-9)}$$

$$A5 = \partial r_{i+1}/\partial z_j = (u_{i+1}\cdot A2 + w_i\cdot A3)/(u_{i+1}^2 + w_i^2)^{1/2} \quad , \qquad \text{(A-10)}$$

$$A6 = \partial R_i/\partial z_j = (u_i\cdot A1 + w_i\cdot A3)/(u_i^2 + w_i^2 + L^2)^{1/2} \quad , \qquad \text{(A-11)}$$

$$A7 = \partial R_{i+1}/\partial z_j = (u_{i+1}\cdot A2 + w_i\cdot A3)/(u_{i+1}^2 + w_i^2 + L^2)^{1/2} \quad , \qquad \text{(A-12)}$$

while the partial derivative of Δg with respect to the density is

$$\partial(\Delta g)/\partial\sigma = G\cdot\sum_{i=1}^{N} 2\cos\phi_i F(i) \quad . \qquad \text{(A-13)}$$